CAMBRIDGE
UNIVERSITY PRESS

RESEARCH ARTICLE

Heavy-duty hexapod robot sideline tipping judgment and recovery

Lianzhao Zhang[1] , Fusheng Zha[1], Wei Guo[1], Chen Chen[2,3], Lining Sun[1] and Pengfei Wang[1]

[1]State Key Laboratory of Robotics and System, Harbin Institute of Technology (HIT), Harbin, China, [2]Heilongjiang Provincial Key Laboratory of Complex Intelligent System and Integration, Harbin University of Science and Technology, Harbin, China, and [3]Key Laboratory of Intelligent Technology for Cutting and Manufacturing Ministry of Education, Harbin University of Science and Technology, Harbin, China
Corresponding authors: Lining Sun; Email: lnsun@hit.edu.cn, Pengfei Wang; Email: wangpengfei@hit.edu.cn

Abstract

Heavy-duty hexapod robots are well-suited for physical transportation, disaster relief, and resource exploration. The immense locomotion capabilities conferred by the six appendages of these systems enable traversal over unstructured and challenging terrain. However, tipping can be a serious concern when moving with a tripod gait in these challenging environments, which may cause irreversible consequences such as compromised movement control and potential damage. In this paper, we focus on heavy-duty hexapod robot sideline tipping judgment and recovery during tripod gait motion, and a novel sideline tipping judgment and recovery method is proposed by adjusting an optimal swinging leg to the stance state. Considering the locomotion environments, motion mode, and tipping analysis, the robot's stability margin is quantified, and the tipping event is evaluated by the Force Angle Stability Measure (FASM). The recovery method is initiated upon detecting that the robot is tipping, which involves the selection of an adjustment leg and the determination of an optimal foothold. Since the FASM is based on the foot force and robot center of gravity (CoG), the stability margin quantification expression is reformulated to the constraint form of quadratic programming (QP). Furthermore, a foot force distribution method, integrating stability margin considerations into the QP model, has been devised to ensure post-adjustment stability of the landing leg. Experiments on tipping judgment and recovery demonstrate the effectiveness of the proposed approaches on tipping judgment and recovery.

1. Introduction

More than 50% of the Earth's land area is characterized by rugged terrain, posing challenges for mobile platforms like wheels and tracks that rely on continuous support. Legged robots offer the advantage of flexible foothold selection, enabling them to traverse harsh terrains such as gullies, slopes, sandy soils, and even swamps with remarkable adaptability and agility [1]. Heavy-duty hexapod robots, in particular, exhibit exceptional load capacity and all-terrain maneuverability, making them highly suitable for applications like mountain transportation and disaster rescue [2–4]. The control algorithm and structure of the robot provide a degree of stability. However, when navigating complex terrain, the limited support area, the large inertia, the external interference, or the small friction coefficient of the ground and other problems make the robot prone to destabilization. To address this issue, it is imperative to establish a method to quantify the robot's stability margin, determine tipping thresholds, and employ appropriate adjustment strategies for tipping recovery of heavy-duty hexapod robots.

As stability is a fundamental prerequisite to ensure safe robotic operation [5, 6], extensive research has focused on quantifying stability margins. Existing criteria can be classified into two main categories: static stability metrics and dynamic stability metrics.

Regarding the measurement of static stability margin, two approaches have been developed. The first approach focuses on the geometric relationship between the CoG and the support polygon. A typical example is the Static Stability Margin (SSM) [7], defined as the minimum CoG projection distance along the gravity vector to the support polygon edge. Since computation of the SSM is complex, the Longitudinal Stability Margin (LSM) is introduced by McGhee et al. [8, 9]. Subsequently, the Crab Longitudinal Stability Margin [10] and Body Longitudinal Stability Margin [11] methods were respectively developed, incorporating appropriate improvements to the LSM. The static stability margin methods mentioned above are calculated solely within the support polygon and do not consider the CoG's height and potential energy. The second approach explores the stability margin from an energy perspective by calculating the minimum amount of gravitational potential energy needed to transition from the current state to a tipped state. Messuri et al. introduced an energy-based method known as Energy Stability Margin (ESM) [12]. However, the ESM is significantly influenced by the robot's mass. To address this concern, Hirose et al. proposed a static stability description method called Normalized Energy Stability Margin (NESM) [13, 14]. Although the NESM eliminates the influence of mass on the stability margin, its fundamental principles are similar to those of the ESM method.

Dynamic stability margin measurement methods can be classified into two main types. The first type is based on the relationship between the equivalence force/moment and constraints, such as the support polygon or stability polyhedron. In this approach, the robot is considered stable if the force remains within the constraints. Otherwise, it is deemed unstable. The Zero Moment Point (ZMP) is a typical dynamic stability margin criteria for legged robots, and it has been modified and applied numerous times to robot stability control, gait planning, foot force distribution, and other robot motion control [15, 16]. Another notable criterion in this category is the FASM [17]. Assuming that the CoG of the robot and the supporting polygon form a stability polyhedron, FASM quantifies the robot's stability margin at a given moment as the minimum angle between the net force at CoG projected on the vertical plane of a side of the stability polyhedron and the vertical line of that side from CoG to support polygon. Building upon FASM, Moosavian and Alipour introduced the Moment-Height Stability (MHS) measure method, primarily used to describe the stability of mobile manipulation robots [18, 19]. Subsequently, researchers proposed additional methods such as Center of Pressure (CoP) [20], Dynamic Stability Margin (DSM) [21], Tumble Stability Margin (TSM) [22], Foot Force Stability Margin (FFSM) [23], and Modified Foot Force Stability Margin (MFFSM) [24]. While FFSM and MFFSM are computationally efficient, they only consider the longitudinal foot-ground contact force and overlook other forces or moments. The second type of dynamic stability margin measurement falls under the energy-based approach. This category aims to quantify the impact of coupled external forces and moments on the robot's stability by employing the ESM. Ghasempoor and Sepehri initially presented the Dynamic Energy Stability Margin (DESM) [25], which was later normalized by Garcia et al., resulting in the Normalized Dynamic Energy Stability Margin (NDESM) [26]. While DESM and NDESM are dynamics-based measures, their implementation can be challenging [24].

Roan et al. [27] conducted a comparative analysis of three stability margin methods – ZMP, FASM, and MHS – on the iRobot PackBot robot, finding FASM and MHS more effective than ZMP, with FASM being the most sensitive and predictive.

Garcia et al. [28] performed an assessment to evaluate the applicability of various stability criteria for legged robot motion. The stability margins are computed and assessed while the robot is walking using a two-phase discontinuous gait under the six different combined conditions – uneven terrain, inertial forces, and external forces. The results are presented in Table I. As illustrated in the first line, the condition "N N N" signifies a horizontal, even terrain in the absence of dynamics, such as lab environments. In this circumstance, NESM and FASM emerge as the optimal criteria as the others do not vary with CoG height. The second line depicts horizontal, even terrain when inertial and elastic effects arise. The FASM is identified as the optimal choice because the static stability margins cannot reflect dynamic effects, while DSM and TSM do not vary with CoG height. In the third line, the NESM and SSM are not applicable as they cannot reflect the influence of manipulation force on stability. In the fourth line, the NESM is the optimal choice because when robot moves on an inclined surface and the CoG is placed at

Table I. *The applicable condition evaluations of typical motion stability criteria. "Y" or "N" denotes the applicability of a criterion, "×," "√," and "∗" indicate conditions that are not applicable, applicable, and the optimal choice, respectively.*

Uneven terrain	Inertial forces	External forces	NESM	SSM	DSM	TSM	FASM
N	N	N	∗	√	√	√	∗
N	Y	N	×	×	√	√	∗
N	Y	Y	×	×	√	√	√
Y	N	N	∗	√	√	√	√
Y	Y	N	×	×	√	√	√
Y	Y	Y	×	×	√	√	√

the maximum NESM point, the possibility of tumbling downhill is equal to uphill. In the fifth and last line, the SSM and NESM do not reflect any reduction of the stability margin due to dynamics. Moreover, it can be discerned from the table that there was no single stability margin criterion that could be universally applied across all circumstances. Each criterion exhibited its own advantages and limitations. These findings emphasize the importance of selecting a suitable robot stability description method by considering factors such as the robot's motion characteristics, intended field of use, and surrounding environment.

Researchers have made significant advancements in robot stability margin measurement, a key component in motion planning [29], trajectory generation [30], and motion control [31], which is crucial for maintaining and enhancing robot stability. However, little attention has been given to addressing tipping recovery mechanisms, especially for the heavy-duty hexapod robot with large inertia, complex motion strategies, and limited leg motion space. Only Peng Saijin et al. [32] have carried out a tipping recovery method, which is inspired by insects. The tipping recovery method is mainly used for small, lightweight hexapod robots, and is used after the robot tips over, which is not suitable for heavy-duty hexapod robots. To bridge this gap, this paper presents a tipping judgment and a recovery methods for a heavy-duty hexapod robot moving in tripod gait, which quantifies and judges the robot stability by FASM and achieving tipping recovery by adjusting optimal leg to stance state with an optimal foot force distribution method inspired by FASM.

The main contributions of this paper are as follows: (1) A sideline tipping judgment method is proposed. The FASM is used to quantify the robot stability margin, and a reasonable instability threshold is set with consideration of the robot's performance to determine tipping events. (2) To our best knowledge, this is the first tipping recovery method for a heavy-duty hexapod robot when moving in tripod gait. Based on the optimal adjustment leg selection strategy, the approximate reachable space calculation method, and the foot force distribution method, the robot's tipping recovery is achieved by adjusting the optimal leg to land on the ground. (3) We show that the proposed judgment method is sensitive to tipping events, and the robot can regain stability after the recovery method is implemented.

The paper is organized as follows: Section 2 provides a system overview and tipping analysis. Section 3 discusses the stability margin quantification and tipping judgment method in detail. Section 4 proposes the detailed tipping recovery method, including adjustment leg selection strategy, reachable space calculation and optimal foothold selection method, and foot force distribution method considering stability. Simulation experiments and the result analysis are carried out in Section 5 to demonstrate the feasibility of the proposed heavy-duty hexapod robot tipping judgment and recovery method. Finally, Section 6 concludes the paper.

2. System overview and tipping analysis

2.1. System overview
The heavy-duty hexapod robot utilized for validating the proposed tipping detection and recovery methods is depicted in Fig. 1. The robot possesses dimensions of 4.7 m in length, 2.5 m in width, and 2 m in
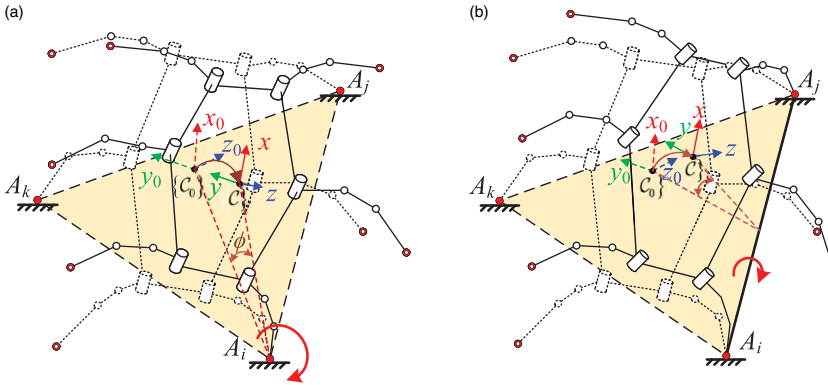
Figure 1. *Robot structure and schematic of FASM. The figure depicts the main reference frames of the robot (world frame {$\mathcal{W}$} and body frame {$\mathcal{C}$}). The stability polyhedron used in FASM is constructed by leg 1, leg 3, leg 5, leg 6, and the CoG collectively, and the $^{B_i}P_G$ is the CoG of the robot. The leg structure is partially decoupled, as in the section view of leg 3.*

height in its initial position. It has a total weight of 5 t, 4.4 t for the body, and 0.1 t for each leg. The robot is mounted with six legs, with the left three legs designated as leg 1, leg 2, and leg 3, and the right three legs as leg 4, leg 5, and leg 6. Each leg has a parallelogram pantograph mechanism structure, which offers superior rigidity and minimal deformation under high loads compared to traditional tandem leg designs. Each leg is facilitated by three electrically actuated joints, horizontal, vertical, and swing joints, employed for controlling the corresponding movements, as shown in Fig. 1. An inertial measurement unit (IMU) is mounted on the robot body to gather crucial information about the robot's physical state. This IMU enables the acquisition of body attitude values such as angular velocities and linear accelerations. Joint position sensors are implemented to capture the joint positions, and 3D contact-force sensors are used to measure the foot-ground contact forces. These sensor inputs, combined with the robot's physical parameters, provide comprehensive measurements of the robot's operational status.

As shown in Fig. 1, {$\mathcal{W}$} is the inertia frame, {$\mathcal{C}$} is the body frame. The Coxa frame of the ith leg is {$\mathcal{B}_i$}, oriented in the same direction as the body frame. The position of the origin of {$\mathcal{B}_i$} in {$\mathcal{C}$} is $l_i = \begin{bmatrix} l_{ix} & l_{iy} & l_{iz} \end{bmatrix}^{\mathrm{T}}$, the ith leg joint position is $J_i = \begin{bmatrix} J_{ix} & J_{iz} & J_{i\theta} \end{bmatrix}^{\mathrm{T}}$, the foot position in Coxa frame of ith leg is $^{B_i}P_i = \begin{bmatrix} ^{B_i}P_{ix} & ^{B_i}P_{iy} & ^{B_i}P_{iz} \end{bmatrix}^{\mathrm{T}}$ and in body frame is $^{C}P_i = \begin{bmatrix} ^{C}P_{ix} & ^{C}P_{iy} & ^{C}P_{iz} \end{bmatrix}^{\mathrm{T}}$. Since the leg structure is partially decoupled, the forward and inverse kinematics of the leg can be obtained through the geometric analysis method. The forward and inverse kinematics in the Coxa frame are expressed as follows:

$$\begin{cases} ^{B_i}P_{ix} = K_x J_{ix} \\ ^{B_i}P_{iy} = L_1 \cos{(J_{i\theta})} + (K_z J_{iz} + L_2) \sin{(J_{i\theta})} \\ ^{B_i}P_{iz} = L_1 \sin{(J_{i\theta})} - (K_z J_{iz} + L_2) \cos{(J_{i\theta})} \end{cases} \tag{1}$$

$$\begin{cases} J_{ix} = \dfrac{^{B_i}P_{ix}}{K_x} \\[4mm] J_{iz} = \dfrac{\sqrt{^{B_i}P_{iy}{}^2 + {}^{B_i}P_{iz}{}^2 - L_1^2 - L_2}}{K_z} \\[4mm] J_{i\theta} = \arcsin{\left(\dfrac{^{B_i}P_{iz}L_1 + {}^{B_i}P_{iy}\sqrt{^{B_i}P_{iy}{}^2 + {}^{B_i}P_{iz}{}^2 - L_1{}^2}}{^{B_i}P_{iy}{}^2 + {}^{B_i}P_{iz}{}^2} \right)} \end{cases} \tag{2}$$

where $K_x = 5$ and $K_z = 4$ represent the scale factor of the horizontal joint and vertical joint, respectively. L_1 represents the distance between the leg plane and the origin of frame {$\mathcal{B}_i$}, with the left leg being positive and the right leg being negative. L_2 represents the distance between the central axes of the horizontal joint and the origin of frame {$\mathcal{B}_i$}.

Figure 2. *Tipping schematic. (a) is corner tipping, and the robot will tip around point A_i. (b) is sideline tipping, and the robot will tip around line A_iA_j.*

2.2. Tipping analysis

As to hexapod robots, tipping can generally occur in two fundamental scenarios, namely corner tipping and sideline tipping, as illustrated in Fig. 2(a) and (b), respectively [33]. Corner tipping refers to the robot rotating around the foot tip of a support leg when tipping, while sideline tipping involves the robot revolving around an edge of the support polygon before overturned. Since corner tipping represents a specific case and is relatively less common than sideline tipping, this investigation focuses primarily on addressing the challenges posed by sideline tipping.

The tipping phenomenon in the robot is characterized by the FASM. Tipping occurs when the minimum angle between the net force at CoG projected on the vertical plane of a side of the stability polyhedron and the vertical line of that side from CoG to support the polygon falls below the threshold set for stability margin. During destabilization, the robot rotates around the straight line formed by the feet of the two supporting legs – these two legs are the effective supporting legs. The two effective support legs can be determined by the foot force in z direction and is verified in Section 5. The forces at the foot of the effective support legs partially counterbalancing the destabilizing force. The remaining unbalanced force induces robot rotation around the edge of the support polygon. Typically, the robot's support polygon is a convex polygon. In the counterclockwise direction, considered as positive, the robot rotates along the edge line following the right-hand rule, resulting in a positive value of ϕ. Furthermore, it is assumed that during tipping, the foot tip forces remain within the friction cone, ensuring that no foot sliding occurs.

3. Stability margin quantification and tipping judgment

According to [28] and considering the motion characteristics of the heavy-duty hexapod robot, tipping events are transient and require stability margin calculation methods that are both effective and rapid. FASM is a highly sensitive dynamic stability margin calculation approach that accounts for external forces, inertial forces, and terrain effects on robot stability. Since the heavy-duty hexapod robot typically operates at relatively low speeds, FASM is well-suited as a stability margin calculation method for this robot type.

Assuming the robot is accelerating, based on D'Alembert's Principle, the equilibrium equations for both the forces and moments acting on the system can be derived as

$$\begin{cases} \sum \boldsymbol{f}_{\text{grav}} + \sum \boldsymbol{f}_{\text{ext}} + \sum \boldsymbol{f}_{\text{sup}} + \sum \boldsymbol{f}_{\text{I}} = 0 \\ \sum \boldsymbol{n}_{\text{grav}} + \sum \boldsymbol{n}_{\text{ext}} + \sum \boldsymbol{n}_{\text{sup}} + \sum \boldsymbol{n}_{\text{I}} = 0 \end{cases} \tag{3}$$

where $\sum f_{\text{grav}}$ and $\sum n_{\text{grav}}$ represent the gravity force and moment generated by gravity, respectively. $\sum f_{\text{ext}}$ and $\sum n_{\text{ext}}$ denote the external disturbance force and moment, respectively. Similarly, $\sum f_{\text{sup}}$ and $\sum n_{\text{sup}}$ correspond to the foot-ground contact force and moment, while $\sum f_{\text{I}}$ and $\sum n_{\text{I}}$ represent the inertial force and inertial moment, respectively.

Based on equation (3), the net force and moment acting on the CoG that destabilize the robot can be expressed as follows:

$$\begin{cases} f_{\text{r}} = \sum f_{\text{grav}} + \sum f_{\text{ext}} + \sum f_{\text{I}} = -\sum f_{\text{sup}} \\ n_{\text{r}} = \sum n_{\text{grav}} + \sum n_{\text{ext}} + \sum n_{\text{I}} = -\sum n_{\text{sup}} \end{cases} \tag{4}$$

For sideline tipping, our primary concern lies in how stable the robot is with respect to the edges of the supporting polygon. Then, the components of f_{r} and n_{r} that destabilizes the robot along the ith edge of the support polygon are

$$\begin{cases} f_{\text{r}i} = \left(E - \hat{a}_i \hat{a}_i^{\text{T}}\right) f_{\text{r}} \\ n_{\text{r}i} = \left(\hat{a}_i \hat{a}_i^{\text{T}}\right) n_{\text{r}} \end{cases} \tag{5}$$

where $E \in \mathbb{R}^{3 \times 3}$ represents the unit matrix, and $\hat{a}_i$ denotes the unite vector along the ith sideline of the support polygon in the counterclockwise direction.

Considering that the FASM quantifies the stability margin as the angle between the projected force and the vertical line, we replace $n_{\text{r}i}$ with an equivalent force couple $n_{\text{r}i}$. As depicted in Fig. 1, leg 1, leg 3, leg 5, leg 6, and the CoG collectively form a stability polyhedron. The equivalent couple relative to the support polygon's edge $\hat{a}_i$ and within the support plane is denoted as

$$f_{ni} = \left(\hat{I}_i \times n_{\text{r}i}\right) / ||I_i|| \tag{6}$$

where $I_i = \left(E - \hat{a}_i \hat{a}_i^{\text{T}}\right) \left({}^{C}P_{i+1} - {}^{C}P_G\right)$ is the vector that passes through the CoG of the robot and is perpendicular to the ith edge of the support polygon, while $\hat{I}_i$ is the unit vector of I_i.

The tipping net force with respect to the ith edge of the supporting polygon is

$$f_i^* = f_{\text{r}i} + f_{ni} \tag{7}$$

The angle between f_i^* and the side corresponding to the edge line of the stability polyhedron is

$$\theta_{bi} = \begin{cases} \arccos\left(\hat{I}_i \cdot f_i^*\right) & \left(\hat{I}_i \cdot f_i^*\right) \cdot \hat{a}_i < 0 \\ -\arccos\left(\hat{I}_i \cdot f_i^*\right) & \text{others} \end{cases} \tag{8}$$

Then, the stability margin of the robot at the current moment is

$$S_{\text{FASM}} = \min_{i=1}^{k} \theta_{bi} \tag{9}$$

where k represents the number of stance legs, with k subsequently being used to represent the number of stance legs.

S_{FASM} quantifies the instantaneous dynamic stability margin of the robot during motion. A higher value of S_{FASM} indicates better stability, with a lower likelihood of instability. Conversely, a lower S_{FASM} suggests poorer stability, with a higher likelihood of instability. In theory, if $S_{\text{FASM}} = 0$, the robot is in a critical stable state. If $S_{\text{FASM}} < 0$, the robot becomes unstable. In our simulations, it is observed that the robot reached a critical unstable state when S_{FASM} is approximately 20. Therefore, the instability threshold, denoted by ξ_f, should be context-specific, where falling below this threshold indicates a loss of stability.

Table II. *Adjustment leg selection when tipping.*

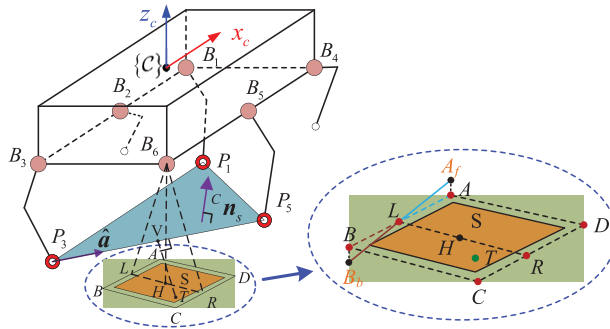| Tipping axis	Leg 1	Leg 2	Leg 3	Leg 4	Leg 5	Leg 6
a_{13}		✓				
a_{35}						✓
a_{51}				✓		
a_{24}	✓					
a_{46}					✓	
a_{62}			✓			

Figure 3. *Adjusting leg reachable space right before tipping. The robot will tip around line P_3P_5, and the figure depicts the reachable space of leg 6. The projected point of point B_6 on the ground is H. L and R are the left and right boundary points. A_f and B_f are the front and rear boundary points, and A and B are the projected point on the ground, respectively.*

4. Tipping recovery based on adjustment of the swing leg

4.1. Adjustment leg selection

In the tripod gait, the robot operates with three legs in the stance phase while the other three legs are in the swinging phase. Referring to the leg numbering in Fig. 2(b), the points A_i, A_j, and A_k represent the foot tip of leg 6, leg 4, and leg 2. During tipping events, the effective support legs are leg 4 and leg 6, while leg 5 is the adjustment leg. To determine the adjustment leg when the robot tips over, consult Table II. In this table, a_{ij} represents the tipping axis formed by the footholds of leg i and leg j, ✓ represents the corresponding leg to be chosen.

4.2. Reachable space calculation and optimal foothold selection

The terrain is fitted using a linear least squares method to enhance computational efficiency, as described in ref. [34]. Let $^C\boldsymbol{n}_s$ denote the unit normal vector of the fitted slope in the body frame, and $^C\boldsymbol{P}'_i$ represent the foot position projection onto the fitted terrain in the body frame. The following calculations and derivations are conducted in the body frame, and "ground" refers to the fitted terrain.

Figure 3 illustrates the schematic diagram of the reachable space for the adjusting leg just before tipping. Points A, B, C, D, L, and R are the boundary points of the reachable space. The swing joint range of motion for the legs is denoted as $J_\theta \in [J_{\theta\,\min}, J_{\theta\,\max}]$. The origin of the leg frame, represented by B_i, is projected onto the ground along the z axis of the body frame to determine point H. Additionally, the maximum length of the leg in the $y_C C z_C$ plane is denoted as $L_{\max}$. If $\left\|\vec{r}_{B_iH}\right\| > L_{\max}$, no viable ground points are identified. If $\left\|\vec{r}_{B_iH}\right\| = L_{\max}$, point H becomes the target location. If $\left\|\vec{r}_{B_iH}\right\| < L_{\max}$, the approximate reachable space of the foot on the ground needs to be solved first and then selects the optimal point. Next, the reachable workspace of the foot on the ground under condition $\left\|\vec{r}_{B_iH}\right\| < L_{\max}$ is derived.

We define $\vec{r}_{HR} \perp \boldsymbol{x}_C$, where $\boldsymbol{x}_C$ represents the unit vector of the body frame in the x direction. Based on geometric relationships, we know that $\vec{r}_{HR} \perp {}^C\boldsymbol{n}_s$, and $\boldsymbol{x}_C$ is the normal vector of the plane B_iHR. The projection of $\boldsymbol{y}_C$ – the unit vector of the body frame in y direction – onto the ground is opposite to $\vec{r}_{HR}$. The angle β between $\vec{r}_{HR}$ and $\vec{r}_{HB_i}$ can be determined using the law of cosines. Let $\vec{r}_{B_iR} = L_{\max}$, the length of $\vec{r}_{HR}$ is

$$\|\vec{r}_{HR}\| = \|\vec{r}_{B_iH}\| \cos \beta + \left(\|\vec{r}_{B_iR}\|^2 - \left(\|\vec{r}_{B_iH}\| \sin \beta \right)^2 \right)^{\frac{1}{2}} \tag{10}$$

The angle of $\angle HB_iR$ can be determined using the law of sines. If $\angle HB_iR < \theta_{\max}$, $\|\vec{r}_{HR}\|$ remains unchanged. If $\angle HB_iR > \theta_{\max}$, set $\angle HB_iR = \theta_{\max}$ and recalculate the length of $\|\vec{r}_{HR}\|$.

To eliminate potential risks, a safety margin $\varrho (1 > \varrho > 0)$ is introduced, and $\|\vec{r}_{HR}\|_{new} = \varrho * \|\vec{r}_{HR}\|$. Then, we can get the position of R

$$ {}^C\boldsymbol{R} = {}^C\boldsymbol{H} + \|\vec{r}_{HR}\|_{new} * \hat{\vec{r}}_{HR} \tag{11}$$

Similarly, the length of $\vec{r}_{HL}$ and the angle of $\angle HB_iL$ can be calculated. If $\angle HB_iL < \theta_{\max}$, its value remains unchanged. If $\angle HB_iL > \theta_{\max}$, let $\angle HB_iL = \theta_{\max}$ and recalculate the length of $\|\vec{r}_{HL}\|$. The position of L is

$$ {}^C\boldsymbol{L} = {}^C\boldsymbol{H} - \varrho * \|\vec{r}_{HL}\| * \hat{\vec{r}}_{HR} \tag{12}$$

Considering that the foot's range of motion is independent in the x direction, assuming that $\vec{r}_{LA_f} = \begin{pmatrix} {}^{Bi}P_{ix\max} & 0 & 0 \end{pmatrix}$ and $\vec{r}_{LB_b} = \begin{pmatrix} {}^{Bi}P_{ix\min} & 0 & 0 \end{pmatrix}$, the projection vectors of them are

$$\begin{cases} \vec{r}_{LA} = \varrho \left(\boldsymbol{1} - {}^C\boldsymbol{n}_s {}^C\boldsymbol{n}_s^{\mathrm{T}} \right) \vec{r}_{LA_f} \\ \vec{r}_{LB} = \varrho \left(\boldsymbol{1} - {}^C\boldsymbol{n}_s {}^C\boldsymbol{n}_s^{\mathrm{T}} \right) \vec{r}_{LB_b} \end{cases} \tag{13}$$

Then, the position of A, B, C, and D can be got.

When the heavy-duty hexapod robot tips around the support polygon edge, the forces exerted by the adjusting leg must counteract the tipping wrench for the robot to regain stability. Considering the relationship between force and torque and aiming to minimize the required force on the foot, the adjusting foothold should be selected from within the reachable workspace on the ground, maximizing the lever arm. Simultaneously, it is crucial to balance reducing adjustment time and minimizing foot force when addressing tipping scenarios in a heavy hexapod robot. A tradeoff between adjustment time and foot force reduction must be carefully considered.

As shown in Fig. 3, segments AB, BC, CD, and DA are generally not parallel to the tipping axis. To prioritize reducing adjustment time and minimizing foot forces, the angle between the foot's reachable space boundary and the tipping axis is calculated. If the angle falls below the threshold value, the R or L point – whichever offers a shorter adjustment time and a more considerable stability margin – as the target footing point. Conversely, when the angle exceeds the threshold, the distance from each boundary point of the reachable space to the tipping axis is calculated, and the point with the largest distance becomes the chosen footing point. Additionally, if point H lies on the tipping axis, the distances from points B and D, A and C, and L and R to the tipping axis are equal. In such cases, we prioritize selecting the point on the right side of the tipping axis. For instance, considering point A, we can use the following formula to determine whether the boundary point is located to the left or right of the tilting axis.

$$\Theta = \vec{r}_{C P_i' A} \times \vec{r}_{C P_i' C P_j'} \cdot \boldsymbol{z}_C \tag{14}$$

where ${}^C P_i'$ represents the first support leg projected onto the fitted terrain along the counterclockwise tipping axis, and ${}^C P_j'$ corresponds to the second support leg. $\boldsymbol{z}_C$ denotes the unit vector of body frame in the z direction. If $\Theta > 0$, point A lies to the right of the tipping axis. Conversely, if $\Theta < 0$, point A is positioned to the left of the tipping axis. Based on this methodology, the adjustment leg target foothold can be determined, denoted as ${}^C\boldsymbol{P}_{tar}$.

When the stability margin falls below the threshold ξ_f, the rate at which the stability margin decreases, denoted as v_s, and the corresponding acceleration, denoted as a_s, can be determined. This information allows us to estimate the time required for the stability margin to decrease from $S_{\text{FASM}} < \xi_f$ to $S_{\text{FASM}} = 0$.

$$t_s = \varkappa \frac{-v_s + \sqrt{v_s^2 - 4a_s \xi_f}}{2a_s} \quad (0 < \varkappa < 1) \tag{15}$$

When the heavy-duty hexapod robot is judged to be tipping, the start position, velocity, and acceleration of the adjusting leg can be determined. After setting the target velocity and acceleration of the adjusting leg, the foot trajectory can be planned using a quintic polynomial. Then, we can get the adjusting leg foot trajectory.

Thus far, we have completed the foothold reachable space calculation and optimal foothold selection.

4.3. Foot force distribution considering stability

To effectively restrain the ongoing instability of the heavy-duty hexapod robot and regain stability upon adjusting leg touchdown while simultaneously preventing damage to the robot caused by internal forces, it is necessary to distribute the foot forces. As the system is overdetermined, it is necessary to introduce additional constraints or define optimization objectives to get an optimal solution. In this context, QP is used to achieve foot force distribution. Notably, the stability margin of the robot, as defined by FASM, is closely linked to foot forces. By integrating QP and FASM, we can consider the robot's stability while obtaining the optimal foot force solution at the moment the adjusting leg makes contact with the terrain.

Considering the high inertia of the heavy-duty hexapod robot, the impact of inertial forces is not negligible, and cannot simplify the calculation of expected force at the CoG as in ref. [35] or [36]. The force and torque in CoG can be formulated as

$$\begin{cases} \boldsymbol{F}_b = -m_b \boldsymbol{a}_b - m_b \mathbf{R}_W^C \boldsymbol{g} \\ \boldsymbol{T}_b = -\boldsymbol{I}\omega_b - \omega_b \times \boldsymbol{I}\omega_b \end{cases} \tag{16}$$

where $\mathbf{R}_W^C \in \mathbb{R}^{3 \times 3}$ represents the transformation from inertial to body frame. $\boldsymbol{I}$ represents the inertia of the body.

To achieve accurate tracking of the desired force and torque at the CoG when mapping the foot forces, the problem can be formulated as

$$\begin{aligned} \min \quad & (\boldsymbol{Ax} - \boldsymbol{b})^{\text{T}} \mathbf{S} (\boldsymbol{Ax} - \boldsymbol{b}) + \kappa \boldsymbol{x}^{\text{T}} \mathbf{W} \boldsymbol{x} \\ \text{s.t.} \quad & Constraints \end{aligned} \tag{17}$$

where $\boldsymbol{A} \in \mathbb{R}^{6k}$ is the transform matrix, and $\boldsymbol{A} = \begin{bmatrix} \boldsymbol{E} & \boldsymbol{E} & \cdots & \boldsymbol{E} \\ {}^C\boldsymbol{P}_1 & {}^C\boldsymbol{P}_2 & \cdots & {}^C\boldsymbol{P}_k \end{bmatrix}$. $\boldsymbol{x} \in \mathbb{R}^{3k}$ is the stance foot force vector. $\boldsymbol{b} \in \mathbb{R}^6$ is the desired force and moment of the robot body. $\mathbf{S} \in \mathbb{R}^{6 \times 6}$ and $\mathbf{W} \in \mathbb{R}^{3k \times 3k}$ are the positive definite weight matrix. κ is the weight factor for the second optimization item.

By transforming equation (17) to the standard form of QP, we can obtain

$$\begin{aligned} \min \quad & \frac{1}{2} \boldsymbol{x}^{\text{T}} \mathbf{U} \boldsymbol{x} + \boldsymbol{f}^{\text{T}} \boldsymbol{x} + \boldsymbol{b}^{\text{T}} \mathbf{S} \boldsymbol{b} \\ \text{s.t.} \quad & Constraints \end{aligned} \tag{18}$$

where $\mathbf{U} \in \mathbb{R}^{3k \times 3k}$ and $\mathbf{U} = 2\boldsymbol{A}^{\text{T}} \mathbf{S} \boldsymbol{A} + 2\kappa W$. $\boldsymbol{f} \in \mathbb{R}^{3k}$ and $\boldsymbol{f}^{\text{T}} = -2\boldsymbol{b}^{\text{T}} \mathbf{S} \boldsymbol{A}$. Since $\boldsymbol{b}^{\text{T}} \mathbf{S} \boldsymbol{b}$ is a constant term and has no effect on the optimization result, it can be ignored.

The constraints in equation (18) are force and stability margin constraints. To ensure the robot's normal operation on the ground, the ground reaction forces in the z direction in the body frame are always positive. It is necessary to prevent sliding between the support feet and the ground. This requires that the tangential force at the robot's feet not exceed the maximum friction force. We adopt the method described in ref. [37] to establish the force constraint for stance feet.
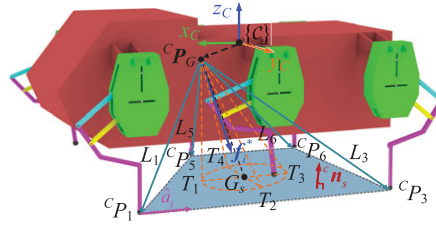
Figure 4. *Stability margin constraint. Based on the geometry relationship, a stability constraint cone with vertex $^C\boldsymbol{P}$ and base $\odot G_s$ is constructed. $\boldsymbol{f}_i^*$ is the net force acting on the CoG. Keeping the $\boldsymbol{f}_i^*$ within the stability constraint cone will be a hard constraint.*

The following step is to obtain the expression for the stability margin constraint. As depicted in Fig. 4, the main idea of the stability margin constraint is to construct a stability constraint cone and then to constrain the net forces acting at the CoG during the FASM calculation to be within the stability constraint cone.

Based on the formulation of (7), the tipping net force in CoG is composed by $\boldsymbol{f}_{ri}$ and $\boldsymbol{f}_{ni}$. Transforming the $\boldsymbol{f}_{ri}$ and $\boldsymbol{f}_{ni}$ to include the foot force vector $\boldsymbol{x}$

$$
\begin{cases}
\boldsymbol{f}_{ri} = -\left(\boldsymbol{E} - \hat{\boldsymbol{a}}_i\hat{\boldsymbol{a}}_i^{\mathrm{T}}\right)\left[\boldsymbol{E}\ \boldsymbol{E}\ \cdots\ \boldsymbol{E}\right]\cdot\boldsymbol{x} \\[2mm]
\boldsymbol{f}_{ni} = -\dfrac{1}{|\boldsymbol{I}_i|}\left(\hat{\boldsymbol{a}}_i\hat{\boldsymbol{a}}_i^{\mathrm{T}}\right)\left[\boldsymbol{T}_1\ \boldsymbol{T}_2\ \cdots\ \boldsymbol{T}_k\right]\cdot\boldsymbol{x}
\end{cases}
\tag{19}
$$

where $\boldsymbol{T}_i$ is the equivalent couples of ith leg, and $\boldsymbol{T}_i = \begin{bmatrix} 0 & -\left(^C P_{iz}' - x_G\right) & {}^C P_{iy}' - y_G \\ {}^C P_{iz}' - z_G & 0 & -\left(^C P_{ix}' - x_G\right) \\ -\left(^C P_{iy}' - y_G\right) & {}^C P_{ix}' - x_G & 0 \end{bmatrix}$.

Based on the idea of FASM, the new formula of net force in CoG is expressed as

$$
\boldsymbol{f}_i^{*\prime} = \boldsymbol{f}_{ri}^{*\prime} + \boldsymbol{f}_{ni}^{*\prime} = -V_i\boldsymbol{x}
\tag{20}
$$

where $V_i \in \mathbb{R}^{3\times 3k}$ is the transform matrix of CoG net force, and $V_i = \left(\mathbf{1} - \hat{\boldsymbol{a}}_i\hat{\boldsymbol{a}}_i^{\mathrm{T}}\right)\left[\boldsymbol{E}\ \boldsymbol{E}\ \cdots\ \boldsymbol{E}\right] + \frac{1}{|\boldsymbol{I}_i|}\cdot\left(\hat{\boldsymbol{a}}_i\hat{\boldsymbol{a}}_i^{\mathrm{T}}\right)\left[\boldsymbol{T}_1\ \boldsymbol{T}_2\ \cdots\ \boldsymbol{T}_k\right]$.

As the support polygon is convex, and the CoG of a triangle is easy to calculate, the centroid $\boldsymbol{G}_s$ of the support polygon can be determined by dividing it into several triangles. Then the minimum value from the $\boldsymbol{G}_s$ to the edges of the support polygon is

$$
d_{\min} = \min\left(\left\|\mathbf{1} - \left\|{}^C\boldsymbol{P}_j' - {}^C\boldsymbol{P}_i'\right\|^{-1}\left({}^C\boldsymbol{P}_j' - {}^C\boldsymbol{P}_i'\right)^{\mathrm{T}}\left({}^C\boldsymbol{P}_j' - {}^C\boldsymbol{P}_i'\right)\left({}^C\boldsymbol{P}_i' - \boldsymbol{G}_s\right)\right\|\right)
\tag{21}
$$

Drawing a circle $\odot G_s$ on the ground with $\boldsymbol{G}_s$ as the center and a radius of $\lambda d_{\min}(1 > \lambda > 0)$. Constructing a stability constraint cone with vertex $^C\boldsymbol{P}_G$ and base $\odot G_s$, as depicted in Fig. 4. The intersection of $\odot G_s$ with the plane perpendicular to the $y_C C z_C$ plane and passing through $^C\boldsymbol{P}_G\boldsymbol{G}_s$ occurs at points $\boldsymbol{T}_1$ and $\boldsymbol{T}_3$. Similarly, the intersection of $\odot G_s$ with the plane perpendicular to the $x_C C z_C$ plane and passing through $^C\boldsymbol{P}_G\boldsymbol{G}_s$ occurs at points $\boldsymbol{T}_2$ and $\boldsymbol{T}_4$. As shown in Fig. 3, the projected unit vector of the y axis of the body frame onto the fitted ground is denoted as $\hat{\vec{r}}_{HR}$. From equation (13), the projected unit vector of the x axis onto the fitted ground is $\hat{\vec{r}}_{LA} = \vec{r}_{LA}/\|\vec{r}_{LA}\|$. Finally, the vectors from the CoG to $\boldsymbol{T}_1$, $\boldsymbol{T}_2$, $\boldsymbol{T}_3$ and $\boldsymbol{T}_4$ can be obtained.

Let $\angle G_s{}^C P_G T_1 = \alpha_1$, $\angle G_s{}^C P_G T_2 = \alpha_2$, $\angle G_s{}^C P_G T_3 = \alpha_3$, $\angle G_s{}^C P_G T_4 = \alpha_4$, and $\alpha_1, \alpha_2, \alpha_3, \alpha_4 \in (0, 90°)$, then we have

$$\tan \alpha_i = \left\| \vec{r}c_{P_G G_s} \times \vec{r}c_{P_G T_i} \right\| / \left| \vec{r}c_{P_G G_s} \cdot \vec{r}c_{P_G T_i} \right| \quad (i = 1, \cdots, 4) \tag{22}$$

For $f_i^{*\prime}$ to be within the stability margin constraint cone, it is necessary to satisfy

$$\sqrt{f_{xi}^{*\prime 2} + f_{yi}^{*\prime 2}} \leq - \tan \alpha_i f_{zi}^{*\prime} \quad (i = 1, \cdots, 4) \tag{23}$$

as $f_i^{*\prime} \leq 0$, the negative sign is added to equation (23).

Equation (23) is a nonlinear inequality. In optimization problems, nonlinear constraints can significantly increase the complexity of the problem. To simplify the nonlinear constraints to linear constraints, we use an inscribed pyramid instead of the stability constraint cone expressed in equation (23). The stability constraint formula of the robot based on the FASM can be expressed as

$$S_M^{\mathrm{T}} V_i x \leq 0 \tag{24}$$

where $S_M = \frac{1}{\sqrt{2}} \begin{bmatrix} \sqrt{2} & 0 & -\sqrt{2} & 0 \\ 0 & \sqrt{2} & 0 & -\sqrt{2} \\ \tan \alpha_1 & \tan \alpha_2 & \tan \alpha_3 & \tan \alpha_4 \end{bmatrix}$ is stability margin constraint transformation matrix.

Putting the constraints into (18), the optimal foot forces vector x is solved after the adjusting leg makes contact with the ground.

5. Simulation experiments and result analysis

Simulation experiments are conducted on the ADAMS-Matlab co-simulation platform to validate the feasibility of the heavy-duty hexapod robot tipping recovery method. The computer used for the simulation is equipped with an Intel Core i5-10400F CPU @ 2.9 GHz hexacore processor and 16 GB RAM. First, the experiment on flat terrain and unilateral cliff terrain walking is carried out to demonstrate the correctness of stability margin measurements and the validity of tipping judgment. Second, tipping experiments in different directions are carried out to demonstrate the effectiveness of the tipping recovery method.

5.1. Stability margin measurement and tipping judgment

To demonstrate the correctness of stability margin measurements and the feasibility of the tipping instability detection method, the hexapod robot is controlled to walk on unilateral cliff terrain with a tripod gait. Initially, the robot moves on flat terrain, after which it moves towards a unilateral cliff terrain where it is expected to tip over. This allows for observing and validating the stability margin and robot state during both stable and unstable conditions. Set the robot to stand for 3 s after starting the simulation to ensure a stable initial state before movement. The duty factor is set to $\beta = 14/24$, the step length is 500 mm for all gaits, the gait cycle is set as T $= 6$ s, and the sample time is 0.02 s.

The variation curves of the CoG position and stability margin, as well as the robot's motion state snapshots, are shown in 5. During the flat terrain movement stage, the position of the CoG in the y axis is 0 due to the robot's symmetry with respect to the $x_C C z_C$ plane of the body frame. Since the robot's movement is periodic, the position of the CoG in the x axis and z axis, and the stability margin of the robot vary periodically. With a duty cycle of $\beta = 14/24$ greater than 0.5, there are moments when all six legs are in a stance state. At $t = 3$ s and $t = 9.4$ s, both represent six legs support states. It can be observed that the robot has the maximum stability margin during the six legs support, with S_{FASM} approximately equal to 48. As the supporting legs move backward, the CoG of the robot moves forward, causing the stability margin to decrease gradually. At $t = 9.7$ s, the robot transitions from a six legs support state to a three legs support state, and the stability margin rapidly decreases with S_{FASM} approximately equal to
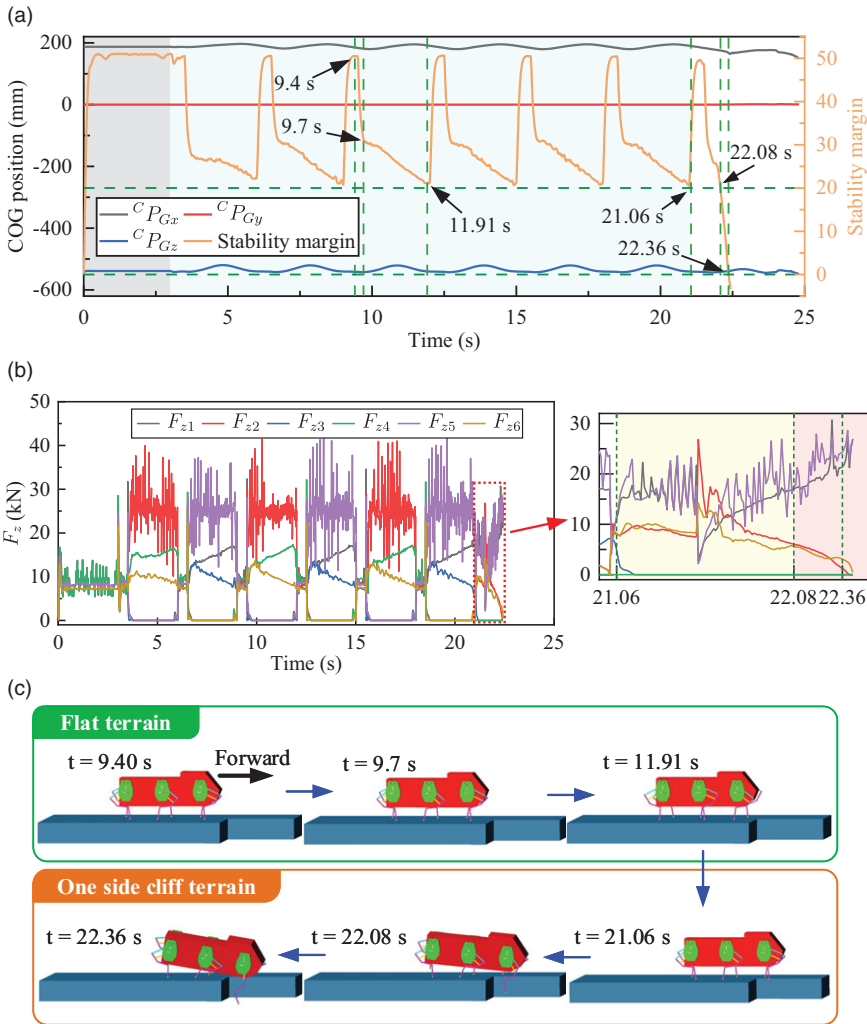
Figure 5. *Robot moves on flat and unilateral cliff terrain. (a) illustrates the CoG position and stability margin curve when robot moving with tripod gait. (b) shows the corresponding z direction feet force curves. (c) depicts the corresponding motion capture snapshots.*

31.41. The corresponding robot state is shown in Fig. 5 (c). When the stance legs reach the rear limits, the stability margin is minimal, and the corresponding robot state is shown in Fig. 5 (c) at $t = 11.91$ s, where the leg is about to transition from swing state to stance state. During the tripod gait, the stability margin of the robot varies periodically in the range of approximately 21–51.

At 21.06 s, leg 4 steps into the void, but the stability margin curve does not show significant fluctuations since the other five legs are still in a supporting state. As the supporting legs continue to move backward, the stability margin remains above 20 for a long time until 22.08 s. At this point, the robot's posture has changed significantly, and the z direction force at the foot of the effective supporting legs (legs 1 and 5) notably exceeds that of the remaining legs, as shown in Fig. 5(b) and (c), indicating that the robot has become unstable. At $t = 22.36$ s, $S_{FASM} = 0$, however, due to the severe change in the robot's posture, as depicted in Fig. 5(c), the stability margin of the robot sharply decreases, and this posture cannot be recovered using an instability recovery strategy. Subsequently, the controller reports an error and stops. To rescue the robot from instability in advance, the criteria given by Papadopoulos cannot be

strictly followed to determine stable or unstable states. Instead, the threshold should be set based on the actual robot to judge instability. In this work, the stability margin threshold is set as $\xi_f = 20$.

5.2. Tipping recovery

Various types of sideline tipping can occur on the hexapod robot, characterized by the change in robot posture and rotation around one edge of the support polygon. To facilitate the validation of the validity of tipping recovery under various conditions and reduce complexity, a 6-UPS Stewart parallel mechanism is established. The heavy-duty hexapod robot is placed on the moving platform of the Stewart platform to establish a combined Stewart-hexapod robot simulation platform, as shown in Fig. 6(a). The radius of the moving platform is 3.5 m, while the fixed platform is 5.5 m. The moving frame $\{\mathcal{A}_s\}$ is attached to the moving platform with the z axis normal to it, and the inertia frame $\{\mathcal{B}_s\}$ is attached to the fixed base with z axis pointing vertically upward. The origins of the two frames, A_s and B_s, are located at the geometric centers of the moving and fixed platforms, respectively. Point b_{si} ($i = 1, 2, \cdots, 6$) is the hinge joint connecting the fixed platform and actuators, while point a_{si} ($i = 1, 2, \cdots, 6$) is the hinge joint connecting the actuators and moving platform. The six actuators are numbered corresponding to their hinge joints, such as $a_{si}b_{si}$ corresponding to actuator i. The minimal length of these actuators is 9 m, and the maximum length of them is 14 m. By controlling the pose of the moving platform, tipping of the robot in different directions can be achieved to verify the effectiveness of the tipping recovery method. The Stewart platform regulates the robot's pose, and the desired functionalities can be achieved through position control. The kinematic analysis of the platform is conducted based on the work in [38].

Control the Stewart platform to rotate counterclockwise about the y axis, rotate clockwise about the y axis, and rotate counterclockwise about the x axis, respectively. These three simulation scenarios simulate the robot's tipping and recovery when climbing a steep slope, descending a steep slope, and moving on a steeply inclined slope at a large angle.

For the robot climbing a steep slope scenario, adjust the robot to the state where legs 1, 3, and 5 are in the stance state. From 0 to 7 s is the robot status adjustment stage when the robot tips with legs 1, 3, and 5 in the stance state, after which the Stewart platform begins rotational motion. The change of the stability margin during the counterclockwise rotation about the y axis of the Stewart platform is shown by the red line in Fig. 6(e) of the top figure, and the red line of the bottom figure shows the corresponding supporting polygon edge. From the top figure of Fig. 6(e), we observe that the stability margin initially increases and then decreases due to the positioning of the robot's center of gravity in the front of the body frame. The backward tipping of the robot causes the net force at the CoG to gradually shift towards the rear, resulting in an increase in the angle between the plane of the support polygon's third edge (formed by the lines connecting leg 1 and leg 5). Simultaneously, the angle between the plane of the support polygon's second edge (formed by the lines connecting leg 3 and leg 5) decreases. However, the minimum angle remains within the plane of the support polygon's third edge. Once the critical value is exceeded, the minimum angle becomes the plane of the second edge of the support polygon. At this point, the Stewart platform continues counterclockwise rotation, and the net force further shifts rearward. The robot stability margin gradually decreases. At 14.48 s, the robot is determined to be about to lose stability when $S_{\text{FASM}} < 20$. At this point, legs 3 and 5 have the maximum leg forces. According to Table II, leg 6 should be selected as the adjustment leg. Based on equation (15), the adjustment time is 0.74 s, with the target foothold point at $(-2390, -1908, -1741)$. After leg 6 lands as a stance leg, the robot stability margin rises from below 20 to around 40, significantly improving stability. The robot state during leg 6 landing as the adjustment leg and the feet force variation curves are shown in Fig. 6(b).

For the robot descending a steep slope, control the Stewart platform to rotate clockwise about the y axis to make the robot tip forward. The stability margin and corresponding support polygon edge variation curves are shown by the green line in the top figure and the black line in the bottom figure of Fig. 6(e). At 11.85 s, the robot is about to lose stability with $S_{\text{FASM}} < 20$. At this point, legs 1 and 5 have the maximum leg forces. Leg 4 should be selected as the adjustment leg, and the adjustment time is 1.0 s with the target foothold point at $(-2490,$
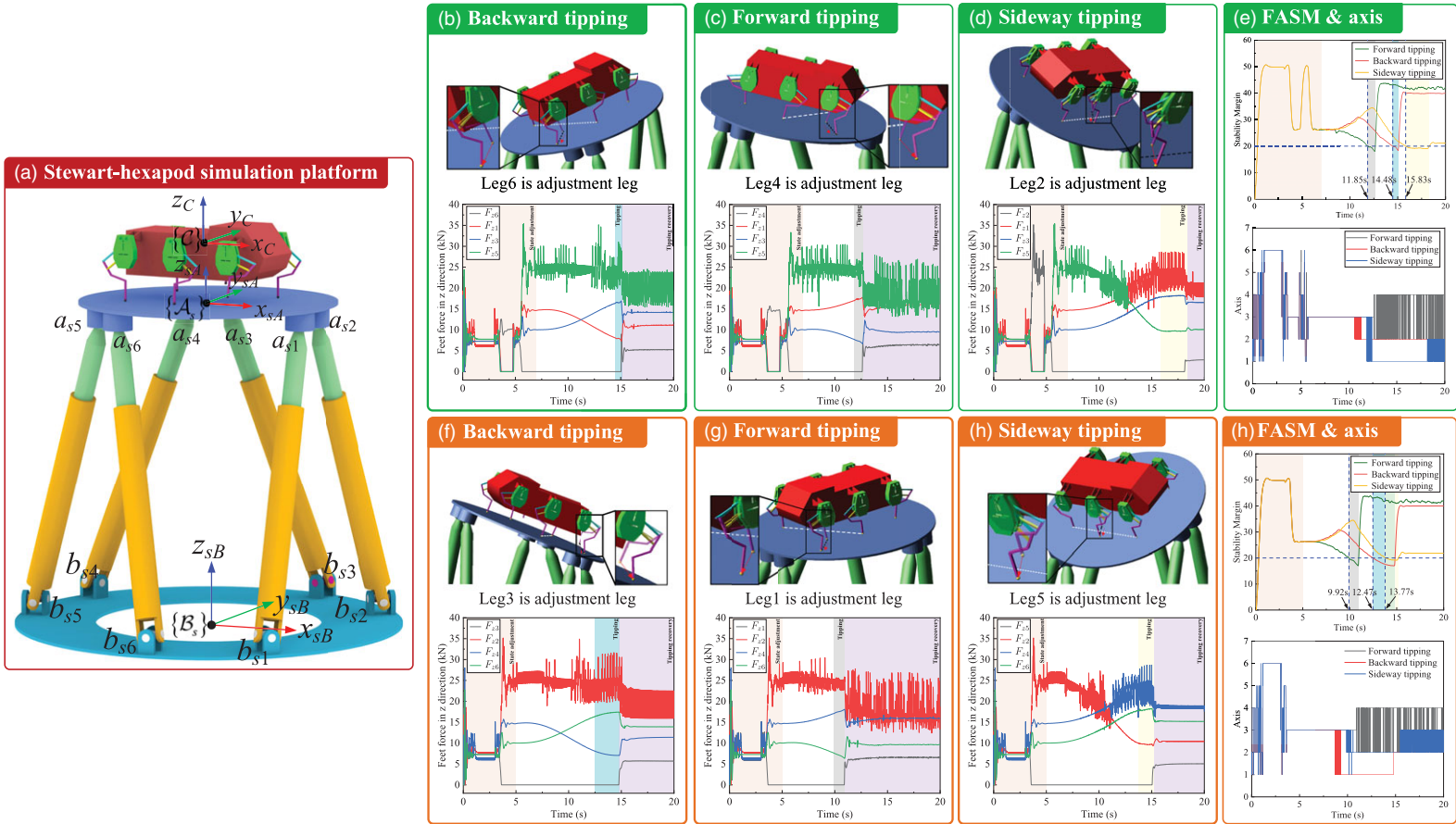
Figure 6. *Stewart-hexapod platform and tipping recovery simulation. (a) represents the combined Stewart-hexapod robot simulation platform, consisting of a 6-UPS Stewart parallel mechanism and the heavy-duty hexapod robot. (b)–(d) illustrate the robot's backward, forward, and sideline tipping recovery with legs 1, 3, and 5 in stance and the corresponding foot force in z direction. The top chart of (e) depicts the stability margin, while the bottom chart depicts the tipping rotation axis. Similarly, (f)–(h) demonstrate the robot's backward, forward, and sideline tipping recovery with legs 2, 4, and 6 stance and the corresponding foot force in z direction. The top chart (i) showcases the stability margin variation curve, and the bottom illustrates the corresponding tipping rotation axis.*

−1908, −1741). After leg 4 lands as a stance leg, the robot stability margin rises from below 20 to around 45, significantly improving stability. The robot state during leg 4 landing as the adjustment leg and the stance feet force curves are shown in Fig. 6(c).

For the scenario of tipping recovery when the heavy-duty hexapod robot moves on a slope with a large inclination angle, control the Stewart platform to rotate counterclockwise around the x axis. The stability margin and corresponding support polygon edge variation curves are shown by the yellow line in the top figure and the blue line in the bottom figure of Fig. 6 (e). At 15.83 s, the robot is about to lose stability with $S_{\text{FASM}} < 20$. Currently, legs 1 and 3 have the maximum force at the foot, and leg 2 should be selected as the adjustment. Based on equation (15), the adjustment time is 2.1 s, with the target foothold point at (0, 1894, −1783). After leg 2 lands as a stance leg, the stability margin of the robot increases from below 20 to about 21.5. The robot's state during leg 2 landing as the adjusting leg and the stance feet force curves are illustrated in Fig. 6 (d).

The recovery of the robot from tipping over when legs 2, 4, and 6 are in the stance state is similar to that when legs 1, 3, and 5 are in the stance state. From 0 to 5 s is the robot status adjustment stage when the robot tips with legs 2, 4, and 6 in the stance state, after which the Stewart platform begins rotational motion.

In the scenario of the robot tipping recovery when climbing a steep slope, the stability margin and corresponding changes in the support polygon's edges during the recovery process are shown by the red line in the top figure of Fig. 6 (i) and by the red line in the bottom figure of it. Leg 3 is selected as the adjustment leg, the adjustment time is 2.31 s with the target foothold point at (−2390, 1908, −1741). The robot state and feet force curves after leg 3 lands on the ground are shown in Fig. 6 (f). In the scenario of the robot tipping recovery when descending a steep slope, the stability margin and corresponding changes in the support polygon's edges during the recovery process are shown by the green line in the top figure and by the black line in the bottom figure of Fig. 6 (i). Leg 1 is selected as the adjustment leg, and the adjustment time is 1.3 s with the target foothold point at (2490, 1913, −1728). The state and the feet force in the z direction of the robot after leg 1 lands on the ground are shown in Fig. 6 (g). In the scenario of the robot tipping recovery when moving on a slope with a large angle of inclination, the stability margin and corresponding changes in the support polygon's edges during the recovery process are shown by the yellow line in the top figure and by the blue line in the bottom figure of Fig. 6 (i). Leg 5 is selected as the adjustment leg, and the adjustment time is 1.48 s with the target foothold point at (0, −1894, −1782). the robot state and stance feet force in z direction after leg 5 lands on the ground are shown in Fig. 6 (h).

Based on the above simulations, it can be observed that the robot is able to achieve tipping recovery according to the pre-designed recovery methods. Particularly in cases of forward and backward tipping instability, the improvement in the robot's stability margin becomes quite evident after the adjustment leg lands. This is primarily because the new stability cone formed after the adjusting leg lands significantly expands the original cone. As to the simulation scenery of moving on a steeply inclined slope at a large angle, although the robot has regained stability, the stability margin is not high. The primary reason is that the range of motion of the leg's swing joint and the maximum length of the leg limit the lateral distance that the foot can reach, preventing the construction of a new, larger stability cone. Therefore, when the robot is moving on a large lateral slope, more attention should be paid to the changes in the robot's stability margin.

6. Conclusion and Prospect

This paper proposes a novel sideline tipping criteria and recovery method for a heavy-duty hexapod robot with a tripod gait by adjusting a swing leg to the stance state. The FASM is used to quantify the stability margin of the heavy-duty hexapod robot, and a reasonable threshold is set to judge the tipping events based on the characteristics of tipping. The unilateral cliff terrain tipping experiment is carried out, and the results show that the FASM is sensitive to variations in robot stability. The stability margin can be quantified effectively by FASM, and the tipping events can be judged in a timely manner. To achieve

adjustment leg landing, an optimal adjustment leg's selection strategy is proposed first. Subsequently, the approximate reachable space of the adjustment leg on fitted ground is calculated, and an optimal foothold is selected. The FASM is reformulated into the form of QP linear constraint, and a foot force distribution method with the consideration of stability margin based on the QP is constructed, which ensures that the robot is stable after the adjustment leg landing. Numerous tipping recovery experiments are conducted, which demonstrate that the optimal adjustment leg can be selected correctly and can land on the target position. After the adjustment leg landing, the robot stability margin increased significantly, allowing the robot to regain stability. This tipping judgment and recovery methods can be applied in various fields, including complex environment logistics and disaster relief. For example, when transporting heavy cargo on rugged terrain, heavy-duty hexapod robots equipped with this instability recovery mechanism can quickly judge and recover from any tipping that may occur during transportation, ensuring the reliability and safety of the transportation task. In the event of a disaster such as an earthquake causing a building to collapse, aftershocks and confined spaces may cause the robot to tip over. This method can quickly restore the robot's stable posture in restricted environments, avoiding interruptions in rescue operations.

However, in this work, we primarily achieve the sideline tipping recovery with tripod gait for the heavy-duty hexapod robot, albeit without considering potential foot slipping during the instability. We will focus on sideline tipping recovery with different gait types and corner tipping recovery in future work and realizing a generalized stabilization approach across diverse operating conditions.

Supplementary material. To view supplementary material for this article, please visit https://doi.org/10.1017/S0263574724000274

References

[1] X. Ding and F. Yang, "Study on hexapod robot manipulation using legs," *Robotica* **34**(2), 468–481 (2016).
[2] H. Yi, Z. Xu, X. Xin, L. Zhou and X. Luo, "Bio-inspired leg design for a heavy-duty hexapod robot," *J. Bionic. Eng.* **19**(4), 975–990 (2022).
[3] M. Agheli, L. Qu and S. S. Nestinger, "SHeRo: Scalable hexapod robot for maintenance, repair, and operations," *Robot. Comput. Interg. Manuf.* **30**(5), 478–488 (2014).
[4] P. Xu, L. Ding, Z. Li, H. Yang, Z. Wang, H. Gao, R. Zhou, Y. Su, Z. Deng and Y. Huang, "Learning physical characteristics like animals for legged robots," *Natl. Sci. Rev.* **10**(5), nwad045(2023).
[5] D. Yang and Y. Liu, "Motion Planning for Hexapod Robot Based on Fitted Curve," *3rd IEEE International Conference on Control Science and Systems Engineering (ICCSSE)* (IEEE, 2017) pp. 205–210.
[6] H. Zhuang, H. Gao, Z. Deng, L. Ding and Z. Liu, "A review of heavy-duty legged robots," *Sci. China Technol. Sci.* **57**(2), 298–314 (2014).
[7] S. Song and K. J. Waldron. *Machines that walk: the adaptive suspension vehicle* (MIT Press, United States, 1989).
[8] R. B. McGhee and G. I. Iswandhi, "Adaptive locomotion of a multilegged robot over rough terrain," *IEEE Trans. Syst. Man Cybernet. B* **9**(4), 176–182 (1979).
[9] Y. Liu and Y. Xu, "Free Gait Planning of Hexapod Robot Based on Improved DQN Algorithm," *IEEE 2nd International Conference on Civil Aviation Safety and Information Technology (ICCASIT)* (IEEE, 2020) pp. 488–491.
[10] S. Song, "Gaits and geometry of a walking chair for the disabled," *J. Terramech.* **26**(3-4), 211–233 (1989).
[11] C. D. Zhang and S. M. Song, "Stability analysis of wave-crab gaits of a quadruped," *J. Robot. Syst.* **7**(2), 243–276 (1990).

[12] D. A. Messuri. "Optimization of the Locomotion of a Legged Vehicle with Respect to Maneuverability (Robot, Walking, Hexapod, Stability)," PhD thesis (The Ohio State University, Columbus, 1985).

[13] S. Hirose, H. Tsukagoshi and K. Yoneda, "Normalized Energy Stability Margin and Its Contour of Walking Vehicles on Rough Terrain," *IEEE International Conference on Robotics and Automation (ICRA)* (IEEE, 2001) pp. 181–186.

[14] H. Chai, Y. Li, R. Song, G. Zhang, Q. Zhang, S. Liu, J. Hou, Y. Xin, M. Yuan and G. Zhang, "A survey of the development of quadruped robots: Joint configuration, dynamic locomotion control method and mobile manipulation approach," *Biomim. Intelli. Robot.* **2**(1), 100029 (2022).

[15] Y. Shi, P. Wang, M. Li, X. Wang, Z. Jiang and Z. Li, "Model Predictive Control for Motion Planning of Quadrupedal Locomotion," *IEEE 4th International Conference on Advanced Robotics and Mechatronics (ICARM)* (IEEE, 2019) pp. 87–92.

[16] M. Mokhtari, M. Taghizadeh and M. Mazare, "Hybrid adaptive robust control based on CPG and ZMP for a lower limb exoskeleton," *Robotica* **39**(2), 181–199 (2021).

[17] E. G. Papadopoulos and D. A. Rey, "A New Measure of Tipover Stability Margin for Mobile Manipulators," *Proceedings of IEEE International Conference on Robotics and Automation* (IEEE, 1996), pp. 3111–3116.

[18] S. Ali, A. Moosavian and K. Alipour, "Stability Evaluation of Mobile Robotic Systems Using Moment-Height Measure," *IEEE Conference on Robotics, Automation and Mechatronics* (IEEE, 2006), pp. 1–6.

[19] X. Ding, Y. Liu, J. Hou and Q. Ma, "Online dynamic tip-over avoidance for a wheeled mobile manipulator with an improved tip-over moment stability criterion," *IEEE Access* **7**, 67632–67645 (2019).

[20] P. Wieber, R. Tedrake and S. Kuindersma, "Modeling and Control of Legged Robots," **In:** *Springer Handbook of Robotics* (B. Siciliano and O. Khatib, eds.) (Springer International Publishing, Berlin, DE, 2016) pp. 1203–1234.

[21] B. S. Lin and S. M. Song, "Dynamic modeling, stability, and energy efficiency of a quadrupedal walking machine," *J. Robot. Syst.* **18**(11), 657–670 (2001).

[22] K. Yoneda and S. Hirose, "Tumble Stability Criterion of Integrated Locomotion and Manipulation," *Proceedings of IEEE/RSJ International Conference on Intelligent Robots and Systems (IROS)* (IEEE, 1996) pp. 870–876.

[23] M. Agheli and S. S. Nestinger, "Foot force based reactive stability of multi-legged robots to external perturbations," *J. Intell. Robot. Syst.* **81**(3-4), 287–300 (2016).

[24] M. Agheli and S. S. Nestinger, "Force-based stability margin for multi-legged robots," *Robot. Auton. Syst.* **83**, 138–149 (2016).

[25] A. Ghasempoor and N. Sepehri, "A Measure of Machine Stability for Moving Base Manipulators," *Proceedings of 1995 IEEE International Conference on Robotics and Automation (IEEE 1995)* (IEEE, 1995) pp. 2249–2254.

[26] E. Garcia and P. G. de Santos, "An improved energy stability margin for walking machines subject to dynamic effects," *Robotica* **23**(1), 13–20 (2005).

[27] A. Irawan and K. Nonami, "Optimal impedance control based on body inertia for a hydraulically driven hexapod robot walking on uneven and extremely soft terrain," *J. Field Robot.* **28**(5), 690–713 (2011).

[28] E. Garcia, J. Estremera and P. G. De Santos, "A comparative study of stability margins for walking machines," *Robotica* **20**(6), 595–606 (2002).

[29] P. Xu, L. Ding, Z. Wang, H. Gao, R. Zhou, Z. Gong and G. Liu, "Contact sequence planning for hexapod robots in sparse foothold environment based on Monte-Carlo tree," *IEEE Robot. Autom. Lett.* **7**(2), 826–833 (2021).

[30] W. Z. Peng, H. Song and J. H. Kim, "Reduced-order Model with Foot Tipping Allowance for Legged Balancing," *International Design Engineering Technical Conferences and Computers and Information in Engineering Conference (American Society of Mechanical Engineers* (American Society of Mechanical Engineers, 2021) pp. V08BT08A011.

[31] Y. Shi, X. He, W. Zou, B. Yu, L. Yuan, M. Li, G. Pan and K. Ba, "Multi-objective optimal torque control with simultaneous motion and force tracking for hydraulic quadruped robots," *Machines* **10**(3), 170 (2022).

[32] S. Peng, X. Ding, F. Yang and K. Xu, "Motion planning and implementation for the self-recovery of an overturned multi-legged robot," *Robotica* **35**(5), 1107–1120 (2017).

[33] H. Tian, Z. Fang, Y. Zhou, S. Li and F. R. Kou, "Analysis and control for tumble stability of wheel-legged robots," *Robot* **31**(2), 159–165 (2009).

[34] J. Xufan. "Research on Compliant Control of Heavy Duty Hexapod Robot Based on Impedance Control," Master thesis (Harbin Institute of Technology, Harbin, 2016).

[35] C. Gehring, S. Coros, M. Hutter, M. Bloesch, M. A. Hoepflinger and R. Siegwart, "Control of Dynamic Gaits for a Quadrupedal Robot," *IEEE International Conference on Robotics and Automation* (IEEE, 2013) pp. 3287–3292.

[36] M. Focchi, A. D. Prete, I. Havoutis, R. Featherstone, D. G. Caldwell and C. Semini, "High-slope terrain locomotion for torque-controlled quadruped robots," *Auton. Robot.* **41**(1), 259–272 (2017).

[37] W. Guanyu, D. Liang, G. Haibo, L. Yiqun, L. Yufei, L. Zhen and D. Zhongquan, "Decomposed QP CFDA for hexapod robots to enhance the slope-climbing ability and experimental validation," *J. Mech. Eng. Sci.* **21**(55), 11–20 (2020).

[38] L. Yanhao, A. Dong, X. Ying, S. Meng, L. Zhenpeng and Z. Defang, "Kinematics analysis of space docking device of 6-UPS Stewart parallel mechanism," *Mach. Tool Hydraul.* **48**(23), 150–154 (2020).